Check for updates

Dynamic arrest of adhesive hard rod dispersions†

Ryan P. Murphy, [a] Harold W. Hatch, [b] Nathan A. Mahynski, [b] Vincent K. Shen[b] and Norman J. Wagner [*a]

The phenomenon of dynamic arrest, more commonly referred to as gel and glass formation, originates as particle motion slows significantly. Current understanding of gels and glasses stems primarily from dispersions of spherical particles, but much less is known about how particle shape affects dynamic arrest transitions. To better understand the effects of particle shape anisotropy on gel and glass formation, we systematically measure the rheology, particle dynamics, and static microstructure of thermoreversible colloidal dispersions of adhesive hard rods (AHR). First, the dynamic arrest transitions are mapped as a function of temperature T, aspect ratio $L/D \approx 3$ to 7, and volume fraction $\phi \approx 0.1$ to 0.5. The critical gel temperature T_{gel} and glass volume fraction ϕ_g are determined from the particle dynamics and rheology. Second, an effective orientation-averaged, short-range attraction between rods is quantified from small-angle scattering measurements and characterized by a reduced temperature τ. Similar τ is found at low rod concentrations, indicating that rod gelation occurs at similar effective attraction strength independent of L/D. Monte Carlo simulations reveal a similar convergence in τ when rods cluster and percolate with an average bond coordination number $\langle n_c \rangle \approx 2.4$, supporting the link between physical gelation and rigidity percolation. Lastly, AHR results are mapped onto a dimensionless state diagram to compare with previous predictions of attraction-driven gels, repulsion-driven glasses, and liquid crystal phases.

1 Introduction

Dynamic arrest transitions of colloidal systems occur from bonding and caging due to intermolecular attractions and excluded volume repulsions.[1,2] Dispersions of spherical particles with short-range attractions (<10% hard core diameter D) often generate kinetically trapped states, gels, and glasses, which can avoid phase separation and crystal formation.[3–6] Practical consequences encompass the gelation of denatured proteins in foods to the vitrification of precipitates in cements.

Investigators of adhesive hard sphere (AHS) model systems have mapped the equilibrium and non-equilibrium states onto a fundamental state diagram.[5,7–14] A well-studied experimental system of octadecyl-coated silica spheres suspended in organic solvents produces thermoreversible gels due to melting transitions of the grafted brush layer.[7,8,12,15,16] When mapped onto a dimensionless state diagram, the attraction-driven gel boundary

extends above the critical point and connects with the attraction-driven glass boundary.[5,12] Simulations identified this gel boundary for physical gelation coincides with an average bond coordination number $\langle n_c \rangle \approx 2.4$,[17] which is consistent with rigidity percolation criterion applied to covalent networks.[18,19]

Previous works on attractive rods have focused on understanding the liquid-crystal phase behavior[20–23] and connectivity percolation,[24,25] but relatively few studies have examined the dynamic arrest of attractive rods.[22,26–30] Moreover, existing experimental approaches define gel and glass boundaries in terms of system-specific units, such as temperature, depletant concentration, or salt concentration. A fundamental, dimensionless state diagram for attractive rods has been hypothesized,[24,26,31,32] but it has not been verified systematically by experiment.

This work proposes a dimensionless state diagram for rod-like particles with short-range attractions, termed adhesive hard rods (AHR). The AHR state diagram extends naturally from the AHS state diagram in the limit where the aspect ratio $L/D = 1$. To distinguish between the coupled attraction-driven and repulsion-driven effects due to the particle shape, this work provides systematic measurements of the non-equilibrium, dynamic arrest transitions as a function of aspect ratio L/D, volume fraction ϕ, and temperature T. First, we use small-amplitude oscillatory shear (SAOS) rheometry and fiber-optic quasi-elasitc light scattering (FOQELS) to define the dynamic

[a] *Center for Neutron Science and Department of Chemical and Biomolecular Engineering, University of Delaware, Newark, Delaware 19716, USA.*
E-mail: wagnernj@udel.edu

[b] *Chemical Informatics Research Group, Chemical Sciences Division, National Institute of Standards and Technology, Gaithersburg, Maryland 20899-83080, USA*

arrest boundaries in terms of a critical gel temperature T_{gel} and critical glass volume fraction ϕ_g for each L/D. Second, we use ultra-small angle X-ray and neutron scattering (USAXS and USANS) to quantify the net, orientation-averaged rod interactions in terms of a reduced temperature τ. Monte Carlo simulations of cylinders with orientation-dependent attractions are performed to validate the orientation-averaged scattering model used to define the net attraction strength τ. Lastly, the gel and glass boundaries are summarized and mapped onto a dimensionless state diagram to compare with previous predictions of dynamic arrest transitions and equilibrium phase boundaries.

2 Experimental methods

2.1 Sample preparation

AHR are composed of octadecyl-coated silica suspended in n-tetradecane. This system allows independent control of L/D and thermoreversible, short-range, van der Waals attractions.[33] Details regarding synthesis and characterization are described in previous work.[33,34] Samples are prepared by suspending dried coated rods in n-tetradecane at $\phi \approx 0.11$ to 0.52 based on particle and solvent densities. Refer to the ESI† for details on sample preparation, supplemental measurements, scattering models, fitting procedures, and parameter sensitivity analysis.

2.2 Small amplitude oscillatory shear rheometry (SAOS)

The frequency-dependent storage modulus (G') and loss modulus (G'') are measured within the linear viscoelastic (LVE) regime by applying a small-amplitude sinusoidal stress and measuring the sinusoidal strain response. Measurements were performed on a DHR-3 stress-controlled rheometer (TA instruments, TRIOS software) equipped with a cone-and-plate geometry, 40 mm diameter cone, 1° cone angle, and a Peltier base plate for temperature control (± 0.1 °C). Additional measurements were performed on a MCR-301 stress-controlled rheometer (Anton Paar) with a cone-and-plate geometry, 50 mm diameter cone, 0.3° cone angle. A solvent trap was filled with tetradecane to mitigate solvent evaporation throughout the rheological measurements.

The thermoreversible, fluid-to-solid transitions of the grafted brushes allow convenient control of the sample shear history by thermal cycling and pre-shearing.[33] Before each measurement, samples were pre-sheared at a constant shear rate $\dot{\gamma} = 10$ s^{-1} for 2 min at 40 °C, cooled to the T of interest, and then equilibrated for 5 min. The LVE regime was determined from sweeping the stress amplitude from $\sigma \approx 10^{-3}$ Pa to 10^2 Pa at a fixed frequency $\omega = 6.28$ rad s^{-1}. Frequency sweeps were performed from high to low frequencies, $\omega = 10^1$ rad s^{-1} to 10^{-1} rad s^{-1}. Sedimentation effects were evident in measurements after ≈ 2 h according to a subtle but systematic decrease in dynamic moduli throughout repeated identical tests. To counteract sedimentation, particles were redistributed by periodically shearing at 20 s^{-1} at 20 °C for 2 min, and then repeating the pre-shear protocol above. The steady-shear viscosity at 40 °C remained consistent between measurements for at least 24 h.

2.3 Fiber-optic quasi-elastic light scattering (FOQELS)

FOQELS measurements were performed with a Brookhaven Instruments Corporation 90-Plus FOQELS instrument with wavelength $\lambda = 635$ nm, source-to-detector scattering angle $\theta = 139°$, magnitude of scattering wavevector $q = 4\pi n \lambda^{-1} \sin(\theta/2) = 0.0027$ Å^{-1}, and a sample pathlength ≈ 1 mm. The employed refractive index of n-tetradecane and silica was 1.429 and 1.456, respectively.[5] The length scale probed ($2\pi q^{-1} \approx 230$ nm) was near the range of rod diameters (200–300 nm) but was less than the estimated mean separation distances $d_{avg} = N_p^{-1/3} \approx 400$–1100 nm, where the particle number density is $N_p \approx 4\phi(\pi D^2 L)^{-1}$. Since $q > 2\pi d_{avg}^{-1}$, measurements probed the self-diffusion.

Sample temperature was controlled with a Peltier chamber and monitored with an external thermocouple to within ± 0.1 °C. To remain consistent with the SAOS pre-shear protocols, sample vials were heated to 40 °C, manually rotated for 2 min, cooled to the desired T, and equilibrated for 5 min before each measurement. Sufficient counts were collected after 2 min, and each measurement was repeated 5 times at a given T to obtain the time-averaged autocorrelation function (ACF) $g^{(2)}(t) - 1$.

The $g^{(2)}(t) - 1$ spanned a delay time, t, from 10^{-5} s to 10^0 s. ACFs were fit with the model following Martin and Wilcoxon[35,36]

$$g^{(2)}(t) - 1 = \beta^2 [Ae^{-\Gamma t} + (1 - A)(1 + t/t^\star)^{(n-1)/2}]^2 \qquad (1)$$

in which β is an amplitude parameter that depends on the instrument geometry, A is the weighting constant between exponential and power-law decay ($0 \leq A \leq 1$), Γ is the single exponential decay constant, $t^\star$ is the characteristic time for transition to power-law decay, and n is the power-law decay exponent ($0 \leq n \leq 1$). The exponential decay relates to the diffusivity of single particles, while the power-law term relates to the diffusion of self-similar clusters.[37] All measurements were fit to eqn (1) using the least squares method and randomly sampled initial conditions bounded by physical limits.

T_{gel} is defined when $n = 0.5$. The average T_{gel} and uncertainty are determined by linear interpolation of the average decay exponent n as a function of the measured temperature T. Error bars in Fig. 2a represent the 95% confidence interval, with a typical uncertainty ± 0.5 °C. Importantly, T_{gel} determined from FOQELS was consistent with T_{gel} determined from SAOS, as defined by the Winter–Chambon criterion at the gel point.[38,39] After repetitive trials of heating, shearing, and quenching the same sample, the time-averaged measurements provided a systematic change in the power-law exponent n with varying T, and thus provided a defining feature of the ergodic to non-ergodic transition.

2.4 Ultra-small angle X-ray and neutron scattering (USAXS and USANS)

USAXS experiments were performed at the Advanced Photon Source on the 9-ID-C USAXS beamline.[40] The slit-smeared scattered intensity was calibrated to an absolute intensity scale and collected over a combined q-range of 0.0001 Å$^{-1} < q < 1$ Å^{-1}, with $q = 4\pi\lambda^{-1} \sin(\theta/2)$, scattering angle θ, incident X-ray wavelengths $\lambda = 0.689$ Å (18 keV) and 0.590 Å (21 keV), and slit lengths 0.0282 Å^{-1} and

0.0334 Å^{-1}, respectively. Samples were syringed into glass capillaries (1.5–1.8 mm OD, 1.1–1.2 mm ID), sealed with wax, equilibrated at 40 °C for 5 min, and then cooled to the temperature of interest. Sample temperature was controlled with a water-cooled temperature stage (± 0.2 °C). Data were reduced to absolute intensities and desmeared using the available packages.[40,41]

USANS experiments were performed at the NIST Center for Neutron Research on the BT5 USANS instrument. The slit-smeared scattered intensity for USANS was collected over a q-range of 0.00004 Å$^{-1} < q < 0.003$ Å^{-1}, with an incident neutron wavelength $\lambda = 2.38$ Å and a slit length 0.117 Å^{-1}. Samples were measured at higher ($T_{high} = 40 \pm 1$ °C) and lower temperatures ($T_{low} = 26 \pm 1$ °C) while slowly rotating the samples to prevent collapse of the suspension microstructure due to gravity.[42,43] Samples measured at $T_{low} = 15.0 \pm 0.1$ °C were instead cooled with a circulating bath and rotated manually. Data were reduced to absolute intensities using available Igor procedures.[44]

The scattering model in eqn (2) was fit using SasView version 4.1.2.[45] The model parameters, parameter sensitivity, uncertainty, and fitting procedures are discussed in detail in the ESI.†

2.5 Monte Carlo simulations (MC)

Wang–Landau MC simulations use an expanded ensemble in attraction strength $\varepsilon/k_B T$ at different L/D and ϕ.[46–48] Orientation-dependent attractions between neighboring cylinders are defined by $U^a/\varepsilon = -\Delta V_{ex}/\Delta V_{ex}^m$, where ΔV_{ex} is the overlap of two cylinder volumes which exclude an implicit hard sphere with a radius $R_g = 0.04D$, and ΔV_{ex}^m is the maximum volume overlap at the potential minimum. MC trials include single-particle translations and rotations, rigid cluster translations and rotations, geometric cluster algorithm,[49] and expanded ensemble changes in. To compute the average bond coordination number $\langle n_c \rangle$ and clusters, pairs of connected particles are defined when their excluded volumes overlap, i.e., when their surfaces are within $2R_g = 0.08D$. For each L/D and ϕ, simulations consist of 3×10^9 to 5×10^{10} MC trials, where averages and standard deviations are from four independent simulations. Additional details are described elsewhere.[46]

3 Results and discussions

3.1 Mapping the gel and glass transitions

Scanning electron microscopy (SEM) images in the inset of Fig. 1 correspond to coated silica rods with average diameters $D \approx 250$ nm to 300 nm, lengths $L \approx 700$ nm to 2000 nm, and $L/D \approx 3$ to 7. Samples are referred to as AR3, AR4, AR6, and AR7 based on their average aspect ratio from SEM (ESI,† Table S1). The desmeared scattering intensities $I(q)$ from ultra small-angle X-ray scattering (USAXS) are shown in Fig. 1 for uncoated rod suspensions in ethanol (open symbols), where $q = 4\pi\lambda^{-1}\sin(\theta/2)$ is the scattering wavevector magnitude, λ is the wavelength, and θ is the scattering angle. Model fits are shown for an orientation-averaged, polydisperse,
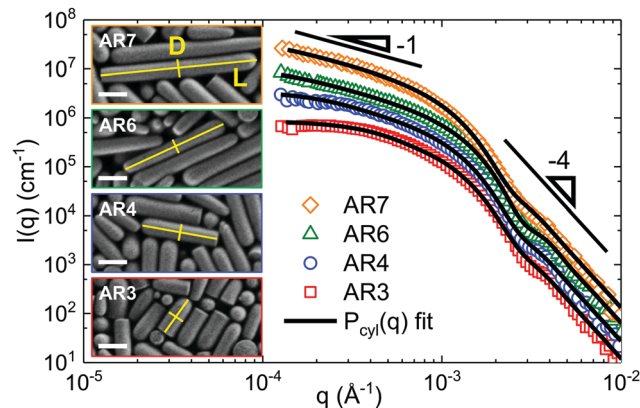

Fig. 1 USAXS of uncoated silica rod suspensions (symbols) and model fits using a polydisperse cylinder form factor $P_{cyl}(q)$ (lines), shifted vertically by 12, 5, 2.5, and 1 (top to bottom). Form factor parameters are listed in ESI,† Table S2. Insets show SEM images of AHR (scale bar 500 nm) with dimensions defined in ESI,† Table S1.

cylinder form factor $P_{cyl}(q)$ (solid lines), which agrees with particle dimensions determined from SEM.[33]

Dynamic arrest boundaries are mapped in Fig. 2a as a function of T, ϕ, and L/D. The critical gel temperatures T_{gel} and glass volume fractions ϕ_g are determined from fiber optic quasi-elastic light scattering (FOQELS, closed symbols) and small amplitude oscillatory shear rheology (SAOS, open symbols). Three pathways highlight dynamic arrest of AR4 from (1) fluid to gel, (2) fluid to glass, and (3) repulsion-driven glass (RDG) to attraction-driven glass (ADG). Although repulsions and attractions both contribute to dynamic arrest, the dominant contributions are distinguished by comparing measurements with variable ϕ at fixed T (repulsion-driven) and with variable T at fixed ϕ (attraction-driven).

Path 1 in Fig. 2a follows the fluid to gel transition of AR4 at $\phi = 0.21$, where $\phi < \phi_g$. FOQELS and SAOS results are shown in Fig. 2b and c, respectively. In Fig. 2b, T_{gel} is defined when the autocorrelation function $g^{(2)} - 1$ transitions from an exponential decay (open squares, 40 °C) to a power-law decay with an exponent $n = 0.5$ (closed blue symbols, $T_{gel} = 25.8 \pm 0.2$ °C). Solid black lines in Fig. 2b and d are fits to the theory from Martin and Wilcoxon (eqn (1)).[35,36] This theory identifies the onset of gelation and consists of a linear weighting of a single exponential decay (single particle diffusion) and a power-law decay (self-similar cluster diffusion). In Fig. 2c, SAOS frequency (ω) sweeps of the storage modulus (G', closed) and loss modulus (G'', open) coincide with the Winter–Chambon definition of the critical gel point,[38] in which $G'(\omega) \sim G''(\omega) \sim \omega^n$ and $n = 0.5$ (blue line, $T_{gel} = 26.0 \pm 1.0$ °C). Thus, FOQELS and SAOS provide a consistent determination of T_{gel} within uncertainty.

Path 2 reveals the fluid to glass transition at 40 °C, where attractions are weakest. FOQELS measurements in Fig. 2d show an abrupt change when $\phi = 0.37 \pm 0.02$ (ϕ_g, blue left triangles), signifying a loss in ergodicity and dynamic arrest into a repulsion-driven glass state.

Path 3 shows the RDG to ADG transition at $\phi = 0.42$, beyond the glass boundary where $\phi > \phi_g$. In contrast to gelation along
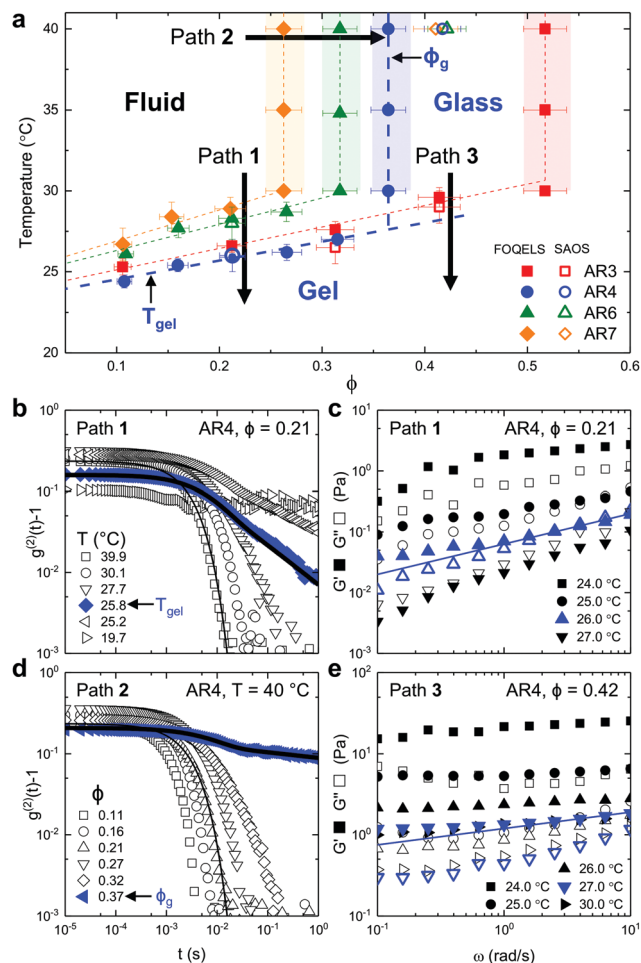
Fig. 2 (a) Critical gel temperatures T_{gel} and glass volume fractions ϕ_g for different aspect ratios (see legend). Dashed lines guide the arrest boundaries determined from FOQELS (closed symbols) and SAOS (open symbols). (b–e) Representative FOQELS or SAOS measurements of AR4 along three paths denoted in (a). Gelation along Path 1 determined from (b) FOQELS autocorrelation functions and (c) SAOS frequency sweeps. (d) Glass transition along Path 2 with increasing ϕ at $T = 40$ °C. (e) RDG to ADG transition along Path 3 at $\phi = 0.42$.

Path 1 at lower ϕ, SAOS frequency sweeps in Fig. 2e show $G' > G''$ for all examined T and ω, as well as a weaker ω dependence (blue line $G' \sim \omega^{0.2}$). The dynamic moduli exhibit a weak T dependence when $T > T_g$, but increase exponentially when $T < T_g \approx 27$ °C. This T-dependent change in dynamic moduli delineates the RDG-ADG transition (ESI,† Fig. S1).

Dispersions of other aspect ratios follow the same trends shown for AR4 (ESI,† Fig. S2) but with systematic shifts in T_{gel} and ϕ_g (ESI,† Fig. S3 and ESI,† Fig. S4). Importantly, AHR and AHS exhibit the same time-dependent, power-law scaling behavior regarding their particle dynamics and dynamic moduli.[5,7,8,12] More specifically, at the critical gel temperature T_{gel}, the autocorrelation function decays with delay time t as a power-law with exponent $n = 0.5$, $g^{(2)}(t) - 1 \sim (1 + t/t^\star)^{-0.5}$ (eqn (1) with $A = 0$). Meanwhile, dynamic moduli grow with frequency ω as a power-law with exponent $n = 0.5$, $G'(\omega) \sim G''(\omega) \sim \omega^{0.5}$. The consistent power-law exponents ($n = 0.5$) for spheres and rods with varying

L/D suggest that dynamic arrest originates from the same underlying mechanism, regardless of the particle geometry. Although this work only examines aspect ratios up to 7, similar power-law scaling ($G'(\omega) \sim G''(\omega) \sim \omega^{0.5}$) was reported for significantly longer rods ($L/D \approx 100$) at much lower rod concentrations ($\phi \approx 0.01$).[28,50] Overall, the distinguishing quantitative effect of L/D is to merely shift the attractive-driven T_{gel} boundary and repulsive-driven ϕ_g boundary.

3.2 Quantifying the average rod interactions

To quantify the interparticle attractions between rods, USAXS and USANS were conducted across a wide range of ϕ and T spanning the arrest transitions. In Fig. 3a, the desmeared USAXS intensity $I(q)$ is shown for AR4 at fixed $T_{low} = 15$ °C (blue symbols, top to bottom $\phi = 0.11$ to 0.52). $I(q)$ is only weakly dependent on T, as shown in Fig. 3b by comparing the slit-smeared USANS intensity at $T_{high} = 40$ °C (red symbols) and $T_{low} = 15$ °C to 27 °C (blue symbols). A comparison of the slit-smeared USANS and USAXS $I(q)$ is shown in ESI,† Fig. S5 and for the full q range in ESI,† Fig. S6.
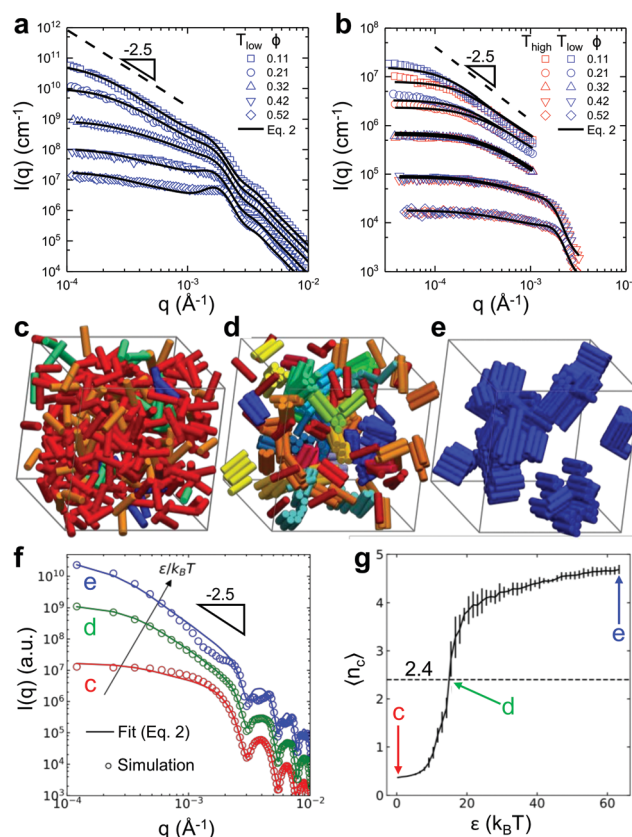

Fig. 3 (a) USAXS of AR4 at $T_{low} = 15$ °C from $\phi = 0.11$ to 0.52 (top to bottom). (b) USANS of AR4 at $T_{high} = 40$ °C (red) and $T_{low} = 15–27$ °C (blue). All curves are vertically shifted by 100, 30, 10, 3, and 1 (top to bottom). (c–e) MC simulations of AR4 with orientation-dependent interaction and increasing attraction strengths ε/k_BT (c) 0.32, (d) 15.44 and (e) 63.44. Red-green-blue color gradient represents increasing number of cylinders in a cluster. (f) Simulated $I(q)$ (symbols) and the model fit to eqn (2) (lines) with $R_{eff} = D/2$, $\delta = 0.074$, and $\tau = 2.166$, 0.115, and 0.101 for c–e, respectively. (g) Corresponding average bond coordination number $\langle n_c \rangle$ obtained from AR4 simulations at $\phi = 0.11$.

Here, a simple scattering model is proposed to quantify the effective, orientation-averaged, short-range attractions between rods in terms of a reduced temperature τ. Using the rigid particle approximation,[31,32] as described in the ESI,† the orientation-averaged scattering intensity $I(q)$ is approximated for an isotropic distribution of rigid cylinders as

$$I(q) \cong N_{cyl}P_{cyl}(q)S_{cm}(q) \qquad (2)$$

in which N_{cyl} is the number density of cylinders, $P_{cyl}(q)$ is the orientation-averaged cylinder form factor (Fig. 1 solid lines), and $S_{cm}(q)$ is the isotropic center-of-mass structure factor. $S_{cm}(q)$ is related to the radial pair distribution function, which describes the relative distribution of particles based on their attractions and repulsions. Within the rigid particle approximation, rods interact as an effective spherical cloud of interaction sites. Thus, the model distinguishes the net orientation-averaged interactions of the collective particle ensemble, but it does not distinguish between local, orientation-dependent interactions.

$S_{cm}(q)$ is fit using the analytical form of the Baxter sticky hard sphere model[51–53] which is described by a reduced temperature $\tau = (12\delta)^{-1} \exp(-U_0/k_BT)$, where $\delta = \Delta/(\Delta + D_{eff})$ is the reduced short-range attraction range, Δ is the small attraction distance, D_{eff} is the effective hard sphere diameter, and U_0 is the attractive potential energy.[12,52–54] Decreasing values of τ correspond to increasing attraction strength or stickiness. Analogous to the reduced second virial coefficient for protein or polymer solutions, the τ parameter characterizes the net, orientation-averaged interactions between all particle pairs.[7,8,12,52,54] Here, the reduced attraction range is fixed at $\delta = 0.01$ based on approximate brush lengths (≈ 3 nm) and core diameters (≈ 300 nm).

The only two fitting parameters include τ and the effective interaction radius R_{eff} ($=D_{eff}/2$). The τ parameter defines the compressibility in the limit of zero scattering angle ($q \rightarrow 0$).[7,8] Model fits are shown in Fig. 3a and b as black solid lines, which capture $I(q)$ for all examined L/D (ESI,† Fig. S7) and all examined ϕ and T (ESI,† Fig. S8). In general, τ increases from approximately 0.1 ($U_0 \approx 4.4\,k_BT$) up to 0.5 ($U_0 \approx 2.8\,k_BT$) with increasing ϕ, while R_{eff} decreases from approximately 230 nm down to 150 nm. The apparent variations in R_{eff} do not significantly affect τ obtained from eqn (2) (ESI,† Fig. S9).

To further test the applicability of the rigid particle approximation and eqn (2), Wang–Landau Monte Carlo (MC) simulations were performed for cylinders with orientation-dependent interactions (Fig. 3c–g). Simulations use an expanded ensemble in attraction strength ε/k_BT at different L/D and ϕ.[46–48] Orientation-dependent attractions between neighboring cylinders are defined by $U^a/\varepsilon = -\Delta V_{ex}/\Delta V_{ex}^m$, where ΔV_{ex} is the overlap of two cylinder volumes which exclude an implicit hard sphere with a radius $R_g = 0.04D$, and ΔV_{ex}^m is the maximum volume overlap at the potential minimum. Although attractions originate from contact forces in experiments, the implicit depletant model in simulations is compared to experiments by assuming the extended theory of corresponding states[54,55] also applies to systems of orientation-averaged anisotropic particles.

MC results for monodisperse cylinders are shown in Fig. 3c–e for $L/D = 4$, $\phi = 0.11$, and increasing ε/k_BT from left to right. The corresponding simulated $I(q)$ (open symbols) and model fit from eqn (2) (solid lines) are shown in Fig. 3f. When attractions are relatively weak (Fig. 3d), eqn (2) shows excellent agreement with $I(q)$ obtained from simulations. However, if excluded-volume repulsions dominate (Fig. 3c) or if strong attractions induce rod alignment (Fig. 3e), then the model deviates from the simulated $I(q)$ at intermediate q. For strong attractions, discrepancies occur near $q = 2\pi D^{-1} \approx 0.002$ Å^{-1} due to the local rod alignment. Additional simulations of bidispersed cylinders confirmed that polydispersity and δ parameters do not significantly affect τ (ESI,† Fig. S10).

As attractions increase, simulations show clustering of locally-aligned rods into bundles. The bundling of rods produces a cluster with higher fractal dimension ($D_f \approx 2.5$), which agrees with experiments. Macroscopic birefringence is not observed under quiescent experiments, which indicates long-range rod alignment does not occur spontaneously. Thus, we speculate that short-range rod bundles exist in experiments, but long-range alignment is hindered by dynamic arrest.

Rod clusters are further characterized by the average bond coordination number $\langle n_c \rangle$ obtained from simulations, as shown in Fig. 3g with increasing attraction strength ε/k_BT. At particular conditions demonstrated in Fig. 3d and f, the scattering model eqn (2) (solid green line) shows the best agreement with the simulated $I(q)$ (open green circles), which occurs approximately when $\langle n_c \rangle \approx 2.4$. This result follows the rigidity percolation criterion for covalent networks,[18,19] which was recently linked to the physical gelation of AHS dispersions.[5,17] The simulations here further support the applicability of rigidity percolation as the underlying mechanism of dynamic arrest for dispersions of attractive rods. The best-fit τ from the isotropic structure factor $S_{cm}(q)$ (eqn (2)) is evaluated at each simulation condition in which the average bond coordination number is ≈ 2.4. The τ values obtained from simulations at all L/D, ϕ, and $\langle n_c \rangle \approx 2.4$ conditions are compared with experiments on a dimensionless state diagram in Fig. 4, which is discussed further in the following section.

3.3 Dimensionless state diagram

By validating that orientation-averaged rod attractions can be quantified with τ, direct comparisons are made possible between spheres and rods on a dimensionless state diagram shown in Fig. 4a. To compare systems with different δ, all results are scaled in terms of the interaction volume fraction $\eta = \phi(1 - \delta)^{-3}$. The τ values from experiments (closed symbols) and from simulations at $\langle n_c \rangle \approx 2.4$ (open symbols) are compared for rods and spheres. Previous results for spheres are shown as black symbols, black lines, and gray regions.[11–14,17,56] The $\tau - \phi$ and $B_2^* - \eta$ plane are shown in the ESI,† for comparison (ESI,† Fig. S11). Error bars represent the standard deviations from repeated measurements and fitting trials.

At low concentrations ($\phi < 0.2$), experiments and simulations of different L/D trend toward the same attraction-driven gel boundary in the $\tau - \eta$ plane. Despite different absolute temperatures T_{gel}
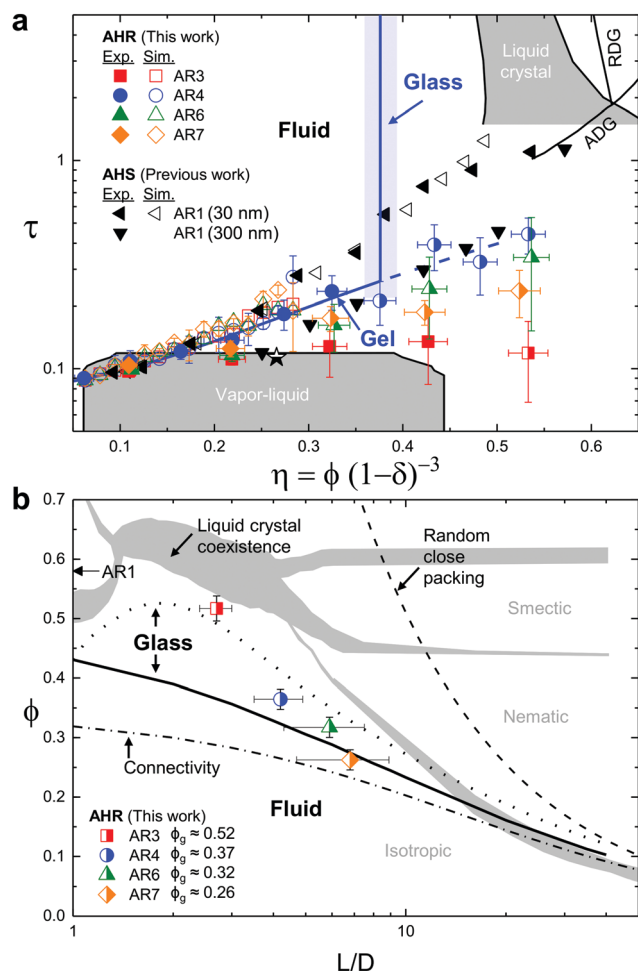
Fig. 4 (a) Dimensionless AHR and AHS state diagrams (see legend). Solid blue lines guide the AR4 gel and glass transitions (closed symbols); dashed line indicates $\phi \geq \phi_g$ (right-filled colored symbols). AHS experiments with $D \approx 30$ nm (closed left triangles),[5] 300 nm (down triangles),[56] MC simulations with $\langle n_c \rangle \approx 2.4$ (open left triangles).[17] The simulated ADG-RDG boundaries (thin black lines)[13] are shifted to higher ϕ to coincide with experimental measurements.[4] Gel and glass boundaries are compared with previous AHS simulations of equilibrium states, including the liquid crystal coexistence (top gray),[14] vapor–liquid binodal (bottom gray),[17] and critical point (bottom-filled star).[11] Refer to ESI† for δ values. (b) Dimensionless hard rod state diagram ($\tau \to \infty$). Measurements of the AHR glass boundary ϕ_g (right-filled symbols) are compared to previous simulations of connectivity percolation of hard spherocylinders (HSC, dot-dashed line, 10% range from eqn (1) in ref. 57), mode-coupling glass of beaded-rods (solid line) and HSC (dotted line),[31] HSC liquid crystals (gray area),[20] and random close packing (dashed line).[58,59] The hard sphere glass ($\phi_g \approx 0.58$)[4] occurs at $L/D = 1$.

(Fig. 2a), the same reduced temperature τ defines dynamic arrest independent of L/D. AHR experiments and simulations are also consistent with adhesive hard sphere results (AR1, $D \approx$ 300 nm, down triangles[56] and $D \approx 30$ nm, left triangles[5,12,17]), which further indicates that the attraction strength required for gelation does not change significantly with L/D.

At high concentrations ($\phi > 0.2$), dynamic arrest transitions become sensitive to L/D, and τ varies non-monotonically with L/D. Since the deviations and uncertainties in τ grow generally

when $\phi \geq \phi_g$ (right-filled symbols), we speculate these deviations in τ emerge as dynamic arrest, liquid crystal formation, and gravitational effects[56] compete at high η.

To closer examine the effects of compaction due to gravity, experimental τ values for rods and spheres are compared as a function of the average particle volume V_p at different ϕ (ESI,† Fig. S12). In general, τ decreases with increasing V_p, which is consistent with observations of adhesive hard spheres with $D \approx 300$ nm.[56] The apparent size-dependent effect was attributed to the competing effects of gravity, where the weight of clusters containing larger particles tend to compact the particle network against Brownian motion.[56] For spheres, network compaction becomes significant when $Pe_g > 0.01$, where Pe_g is a gravitational Péclet number given by the ratio of characteristic time for cluster diffusion to sedimentation.[56] For rods, a similar compaction front (gel syneresis) is observed over several hours when approximately $\phi < 0.3$ and $Pe_g > 0.1$. Since the measurements in this work actively mitigated sedimentation effects, more quantitative measurements are necessary to understand the compaction of AHR gels.

Lastly, to compare with predictions of liquid-crystal and glass boundaries for hard rods, measurements of ϕ_g corresponding to the glass transition are shown in Fig. 4b in the ϕ–L/D plane. Measurements of ϕ_g (right-filled symbols) show reasonable agreement between the simulated ideal glass boundaries of hard spherocylinders (dotted line) and beaded-rods (solid line) obtained from mode-coupling theories and rigid particle approximations.[31,32] The rigid rod ideal glass boundary resides between previous predictions of connectivity percolation (dot-dashed line, 10% D connectivity distance)[57] and random close packing (dashed line, $\phi = 5.1(L/D)^{-1}$).[58,59] Notably, ϕ_g resides below the simulated isotropic–nematic coexistence boundary for hard spherocylinders (gray area);[20,21] however, liquid crystal formation[21] and connectivity percolation[24] are predicted to decrease in ϕ with addition of short-range attractions.

4 Conclusions

The dynamic arrest transitions of adhesive hard rod dispersions are systematically measured as a function of T, ϕ, and L/D. In Section 3.1, the microscopic particle dynamics and macroscopic dynamic moduli of AHR dispersions exhibit similar power-law scaling behavior at the critical gel temperature T_{gel}. The consistent in power-law exponents ($n = 0.5$) from FOQELS and SAOS measurements at different L/D suggest that dynamic arrest originates from the same underlying mechanism, regardless of the particle geometry. The key quantitative effect of L/D is to shift the attractive-driven gel boundary T_{gel} and the repulsive-driven glass boundary ϕ_g.

In Section 3.2, the average rod attractions are quantified using a simple scattering model (eqn (2)) that describes the net, orientation-averaged attraction in terms of a reduced temperature τ. Monte Carlo simulations of cylinders with orientation-dependent attractions further validate the scattering model, and τ values

obtained from simulations at the rigidity percolation criterion ($\langle n_c \rangle \approx 2.4$) are in good agreement with experimental τ values at low rod concentrations.

Lastly in Section 3.3, the dynamic arrest transitions of adhesive hard rod dispersions are mapped onto a dimensionless state diagram and compared with previous predictions of dynamic arrest boundaries and equilibrium phase boundaries. At lower rod concentrations, AHR experiments and simulations demonstrate that the attraction-driven gel boundary (τ) does not vary significantly with L/D. Thus, despite different attraction ranges and interaction potentials, AHR experiments and simulations demonstrate that the orientation-averaged attraction strengths (τ) are consistent at the dynamic arrest boundary. These results support the extended theory of corresponding states as applied to orientation-averaged systems of anisotropic particles with short-range attractions, at least for the modest aspect ratios examined in this work. An extension of this work is necessary to determine if corresponding state concepts apply in the limit of large aspect ratios ($L/D \gg 10$).

At higher rod concentrations, dynamic arrest becomes sensitive to L/D. We speculate the deviations in τ occur as liquid crystal formation competes with repulsion-driven glass formation, particularly at concentrations when $\phi \geq \phi_g$. The repulsion-driven glass boundary ϕ_g is strongly dependent on L/D, and AHR measurements are in reasonable agreement with previous mode-coupling simulations.[31,32] Notably, the AHR ϕ_g boundary precedes the isotropic–nematic transition predicted for hard spherocylinders.[20]

Further investigations are required to distinguish between the competing processes of gelation, phase separation, and gravitational collapse at lower ϕ, and to distinguish between the competition of liquid crystal and glass formation at higher ϕ. Building upon this fundamental state diagram will provide useful reference states to understand the kinetic arrest of more complex molecules, polymers, proteins, and anisotropic colloids with short-range interactions.

Conflicts of interest

There are no conflicts to declare.

Acknowledgements

References

1 E. Zaccarelli, *J. Phys.: Condens. Matter*, 2007, **19**, 323101.
2 E. Zaccarelli and W. C. K. Poon, *Proc. Natl. Acad. Sci. U. S. A.*, 2009, **106**, 15203–15208.
3 P. J. Lu, E. Zaccarelli, F. Ciulla, A. B. Schofield, F. Sciortino and D. A. Weitz, *Nature*, 2008, **453**, 499–503.
4 K. N. Pham, A. M. Puertas, J. Bergenholtz, S. Egelhaaf, A. Moussaid, P. N. Pusey, A. B. Schofield, M. E. Cates, M. Fuchs and W. C. K. Poon, *Science*, 2002, **296**, 104–106.
5 A. P. R. Eberle, N. J. Wagner and R. Castaneda-Priego, *Phys. Rev. Lett.*, 2011, **106**, 105704.
6 M. Kohl, R. F. Capellmann, M. Laurati, S. U. Egelhaaf and M. Schmiedeberg, *Nat. Commun.*, 2016, **7**, 11817.
7 H. Verduin and J. K. G. Dhont, *J. Colloid Interface Sci.*, 1995, **172**, 425–437.
8 M. C. Grant and W. B. Russel, *Phys. Rev. E*, 1993, **47**, 2606–2614.
9 D. Rosenbaum, P. C. Zamora and C. F. Zukoski, *Phys. Rev. Lett.*, 1996, **76**, 150–153.
10 E. Zaccarelli, S. V. Buldyrev, E. La Nave, A. J. Moreno, I. Saika-Voivod, F. Sciortino and P. Tartaglia, *Phys. Rev. Lett.*, 2005, **94**, 218301.
11 M. A. Miller and D. Frenkel, *Phys. Rev. Lett.*, 2003, **90**, 135702.
12 A. P. R. Eberle, R. Castaneda-Priego, J. M. Kim and N. J. Wagner, *Langmuir*, 2011, **28**, 1866–1878.
13 J. Bergenholtz and M. Fuchs, *Phys. Rev. E*, 1999, **59**, 5706–5715.
14 D. W. Marr and A. P. Gast, *J. Chem. Phys.*, 1993, **99**, 2024–2031.
15 S. Roke, O. Berg, J. Buitenhuis, A. van Blaaderen and M. Bonn, *Proc. Natl. Acad. Sci. U. S. A.*, 2006, **103**, 13310–13314.
16 A. P. R. Eberle, N. J. Wagner, B. Akgun and S. K. Satija, *Langmuir*, 2010, **26**, 3003–3007.
17 N. E. Valadez-Pérez, Y. Liu, A. P. R. Eberle, N. J. Wagner and R. Castaneda-Priego, *Phys. Rev. E*, 2013, **88**, 060302(R).
18 H. He and M. F. Thorpe, *Phys. Rev. Lett.*, 1985, **54**, 2107–2110.
19 D. J. Jacobs and M. F. Thorpe, *Phys. Rev. Lett.*, 1995, **75**, 4051–4054.
20 P. Bolhuis and D. Frenkel, *J. Chem. Phys.*, 1997, **106**, 666–687.
21 P. G. Bolhuis, A. Stroobants, D. Frenkel and H. N. W. Lekkerkerker, *J. Chem. Phys.*, 1997, **107**, 1551.
22 R. Ni, S. Belli, R. van Roij and M. Dijkstra, *Phys. Rev. Lett.*, 2010, **105**, 088302.
23 S. V. Savenko and M. Dijkstra, *J. Chem. Phys.*, 2006, **124**, 234902.
24 M. Dixit, H. Meyer and T. Schilling, *Phys. Rev. E*, 2016, **93**, 012116.
25 T. Schilling, S. Jungblut and M. A. Miller, *Phys. Rev. Lett.*, 2007, **98**, 108303.

26 M. J. Solomon and P. T. Spicer, *Soft Matter*, 2010, **6**, 1391–1400.

27 G. M. Wilkins, P. T. Spicer and M. J. Solomon, *Langmuir*, 2009, **25**, 8951–8959.

28 N. K. Reddy, Z. Zhang, M. P. Lettinga, J. K. G. Dhont and J. Vermant, *J. Rheol.*, 2012, **56**, 1153–1174.

29 A. M. Wierenga, A. P. Philipse and H. N. W. Lekkerkerker, *Langmuir*, 1998, **14**, 55–65.

30 R. Chelakkot, R. Lipowsky and T. Gruhn, *Soft Matter*, 2009, **5**, 1504.

31 G. Yatsenko and K. S. Schweizer, *J. Chem. Phys.*, 2007, **126**, 014505.

32 R. Jadrich and K. S. Schweizer, *J. Chem. Phys.*, 2011, **135**, 234902.

33 R. P. Murphy, K. Hong and N. J. Wagner, *Langmuir*, 2016, **32**, 8424–8435.

34 R. P. Murphy, K. Hong and N. J. Wagner, *J. Colloid Interface Sci.*, 2017, **501**, 45–53.

35 J. E. Martin and J. P. Wilcoxon, *Phys. Rev. Lett.*, 1988, **61**, 373–376.

36 J. E. Martin, J. Wilcoxon and J. Odinek, *Phys. Rev. A: At., Mol., Opt. Phys.*, 1991, **43**, 858–872.

37 S. L. Elliott, R. J. Butera, L. H. Hanus and N. J. Wagner, *Faraday Discuss.*, 2003, **123**, 369–383.

38 H. H. Winter and F. Chambon, *J. Rheol.*, 1986, **30**, 367–382.

39 F. Chambon, Z. S. Petrovic, W. J. MacKnight and H. H. Winter, *Macromolecules*, 1986, **19**, 2146–2149.

40 J. Ilavsky, P. R. Jemian, A. J. Allen, F. Zhang, L. E. Levine and G. G. Long, *J. Appl. Crystallogr.*, 2009, **42**, 469–479.

41 J. Ilavsky and P. R. Jemian, *J. Appl. Crystallogr.*, 2009, **42**, 347–353.

42 A. Olsson, M. S. Hellsing and A. R. Rennie, *Meas. Sci. Technol.*, 2013, **24**, 105901.

43 J. B. Leao, R. P. Murphy, N. J. Wagner and M. Bleuel, *J. Neutron Res.*, 2017, **19**, 23–26.

44 S. R. Kline, *J. Appl. Crystallogr.*, 2006, **39**, 895–900.

45 M. Doucet, J. H. Cho, G. Alina, J. Bakker, W. Bouwman, P. Butler, K. Campbell, M. Gonzales, R. Heenan, A. Jackson, P. Juhas, S. King, P. Kienzle, J. Krzywon, A. Markvardsen, T. Nielsen, L. O'Driscoll, W. Potrzebowski, R. Ferraz Leal, T. Richter, P. Rozycko, T. Snow and A. Washington, http://www.sasview.org/, 2016.

46 H. W. Hatch, N. A. Mahynski, R. P. Murphy, M. A. Blanco and V. K. Shen, *AIP Adv.*, 2018, **8**, 095210.

47 H. W. Hatch, W. P. Krekelberg, S. D. Hudson and V. K. Shen, *J. Chem. Phys.*, 2016, **144**, 194902.

48 H. W. Hatch, N. A. Mahynski and V. K. Shen, *J. Res. Natl. Inst. Stand. Technol.*, 2018, **123**, 123004.

49 J. Liu and E. Luijten, *Phys. Rev. Lett.*, 2004, **92**, 035504.

50 R. Zhang and K. S. Schweizer, *Phys. Rev. E: Stat., Nonlinear, Soft Matter Phys.*, 2009, **80**, 011502.

51 R. J. Baxter, *J. Chem. Phys.*, 1968, **49**, 2770–2774.

52 Y. C. Chiew and E. D. Glandt, *J. Phys. A: Math. Gen.*, 1983, **16**, 2599–2608.

53 S. V. G. Menon, C. Manohar and K. S. Rao, *J. Chem. Phys.*, 1991, **95**, 9186–9190.

54 M. G. Noro and D. Frenkel, *J. Chem. Phys.*, 2000, **113**, 2941.

55 G. Foffi and F. Sciortino, *J. Phys. Chem. B*, 2007, **111**, 9702–9705.

56 J. M. Kim, J. Fang, A. P. R. Eberle, R. Castaneda-Priego and N. J. Wagner, *Phys. Rev. Lett.*, 2013, **110**, 208302.

57 T. Schilling, M. A. Miller and P. van der Schoot, *EPL*, 2015, **111**, 56004.

58 A. P. Philipse, *Langmuir*, 1996, **12**, 1127–1133.

59 S. R. Williams and A. P. Philipse, *Phys. Rev. E: Stat., Nonlinear, Soft Matter Phys.*, 2003, **67**, 051301.